Industrial Crops & Products 246 (2026) 123404

Contents lists available at ScienceDirect

Industrial Crops & Products

journal homepage: www.elsevier.com/locate/indcrop

Bamboo-derived carbon induced self-assembly of Mg-modulated Ni–Co layered hydroxide heterostructures for high-performance asymmetric supercapacitors

Menghan Li [a,1], Qianqian Zhang [a,1], Zhiying Lin [a], Qingcai Cai [a], Lu Luo [b,*], Jiawei Qiang [c], Jiuping Rao [a], Mizi Fan [a], Weigang Zhao [a,*], Qinzhi Zeng [a,*]

[a] College of Material Engineering, Fujian Agriculture and Forestry University, 63 Xiyuangong Road, Fuzhou 350002, PR China
[b] School of Naval Architecture and Maritime, Zhejiang Ocean University, 1 Haidanan Road, Zhoushan 316022, PR China
[c] College of Chemistry, Beijing Normal University, 19, Xinjiekouwai St, Haidian District, Beijing 100875, PR China

ARTICLE INFO

Keywords:
Bamboo biomass
Biomass valorization
Bamboo-derived carbon
Layered hydroxides
Asymmetric supercapacitors
Sustainable materials

ABSTRACT

Bamboo is an abundant and fast-growing lignocellulosic resource with considerable potential as a sustainable precursor for functional carbon materials. In this work, bamboo-derived carbon microspheres were employed to induce the self-assembly of Mg-modulated Ni-Co layered hydroxide heterostructures, forming a hierarchical composite electrode denoted as NCM@BC. During synthesis, the carbon microspheres acted not only as conductive supports but also as heterogeneous nucleation sites for hydroxide growth, leading to an open architecture that facilitated electrolyte penetration and charge transport. Meanwhile, Mg incorporation regulated the local coordination environment of the Ni-Co hydroxide phase and improved the structural stability of the layered framework during repeated redox reactions. As a result, the optimized NCM@BC-20 electrode delivered a specific capacitance of 1226.8 F g^{-1} at 1 A g^{-1} with favorable rate capability. Furthermore, the assembled asymmetric supercapacitor, using NCM@BC-20 as the positive electrode and activated carbon as the negative electrode, operated over a 1.6 V voltage window, achieved an energy density of 63.16 Wh kg^{-1} at 800 W kg^{-1}, and retained 89.1% of its peak capacitance after 6000 cycles. These results demonstrate that bamboo biomass can be converted into a value-added carbon component that not only directs heterostructure formation but also contributes to enhanced electrochemical performance, providing a practical route for the development of sustainable carbon-based electrode materials.

1. Introduction

The worldwide rise in energy consumption, together with increasingly severe environmental pressures, has accelerated the pursuit of efficient and sustainable energy-storage technologies (Huang et al., 2025; Tavakoli et al., 2025). Renewable resources, particularly solar and wind energy, are regarded as key options for building low-carbon energy systems (Braff et al., 2016). However, the fluctuating and weather-dependent nature of these resources poses a major challenge to stable and continuous power delivery (Guerra et al., 2020). In response to this challenge, supercapacitors have been extensively investigated as efficient electrochemical energy-storage devices (Seenivasan et al., 2025; Zhao et al., 2026). Their storage behavior can generally be divided into two categories (Wang et al., 2023a; Kumar et al., 2021). Electric double-layer capacitors (EDLCs) operate through electrostatic ion accumulation at the electrode/electrolyte interface, whereas pseudocapacitors depend on fast Faradaic reactions (Tang et al., 2024). Although EDLCs generally exhibit outstanding rate capability and cycling lifespan, their energy density is still limited because charge storage mainly relies on interfacial ion adsorption on carbon surfaces (Nithya, 2021). In comparison, pseudocapacitors offer greater potential for enhanced capacitance and energy density (Cheng et al., 2021). Among the various pseudocapacitive materials reported to date, transition-metal layered hydroxides are considered promising pseudocapacitive materials because they offer abundant redox-active states, tunable compositions, and high theoretical capacitance (Zhao et al., 2025; Maity et al., 2020).

* Corresponding authors.
E-mail addresses: lu-luo@zjou.edu.cn (L. Luo), weigang-zhao@fafu.edu.cn (W. Zhao), fjafuzqz@163.com (Q. Zeng).
[1] These authors contributed equally to this work.

https://doi.org/10.1016/j.indcrop.2026.123404
Received 21 March 2026; Received in revised form 23 April 2026; Accepted 2 May 2026
Available online 9 May 2026

Nevertheless, their practical application is still hindered by slow charge-transfer kinetics, poor intrinsic electrical conductivity, and structural degradation during repeated redox cycling (Huang et al., 2018).

Nickel- and cobalt-based materials are representative pseudocapacitive electrodes due to their rich redox chemistry and relatively high intrinsic conductivity compared with other transition-metal compounds (Zhang et al., 2024; Wang et al., 2025a). Nevertheless, monometallic Ni- or Co-based electrodes commonly suffer from limited rate capability and rapid capacity fading, primarily resulting from constrained ion diffusion pathways and severe structural degradation during cycling (Chen et al., 2020; Tang et al., 2022). To address these challenges, bimetallic systems such as Ni-Co- and Ni-Mn-based materials have been extensively explored (Zhang et al., 2024; Chen et al., 2025), in which the synergistic interaction between different metal cations enables improved redox activity, enhanced charge transport, and better cycling stability. Despite these advances, bimetallic systems still face inherent limitations, including restricted structural tunability and insufficient durability under high current densities (Luo et al., 2022).

Extending bimetallic systems to ternary compositions is an effective way to further enhance electrochemical performance (Lan et al., 2024). Rather than simply increasing the number of redox-active centers, multimetal synergy provides additional degrees of freedom to regulate electronic structure, defect chemistry, and charge-transfer pathways (Xia et al., 2016). Under mild hydrothermal or solvothermal conditions with controlled OH^- release (e.g., urea-assisted precipitation), such multimetal systems preferentially evolve into layered double hydroxide (LDH)-type structures rather than fully crystallized oxides. LDH-type materials feature intrinsically open layered frameworks, tunable metal compositions, and abundant electrochemically accessible sites, rendering them particularly attractive for pseudocapacitive energy storage (Wang et al., 2025a; He et al., 2025a). Notably, beyond the incorporation of additional redox-active elements, introducing electrochemically inactive metal species offers an alternative route to regulate structure and kinetics without compromising cycling stability. In this regard, magnesium (Mg) represents an attractive yet underexplored component. Although Mg^{2+} does not directly participate in Faradaic reactions within the relevant potential window, previous studies have shown that Mg incorporation can stabilize Ni/Co hydroxide microstructures, regulate nanosheet growth, and improve long-term cycling stability in related hydroxide-based supercapacitor electrodes (Yao et al., 2023a, 2023b). The studies have proved that the Mg can primarily function as a structural and microstructural modulator rather than as an additional redox-active center (Xie et al., 2018; Yin et al., 2019). Moreover, it is well established that Ni/Co-based LDH electrodes undergo reversible surface reconstruction in alkaline electrolytes, forming highly active oxyhydroxide species that dominate pseudocapacitive charge storage (Wang et al., 2023b, 2025a). Therefore, rational design of ternary LDH systems with controlled composition and microstructure is essential for achieving high-performance supercapacitors.

However, the practical use of ternary LDH materials is still restricted by low intrinsic conductivity and unsatisfactory mechanical stability, especially under fast-charging and long-term cycling conditions. Integrating LDH-based materials with conductive matrices has thus been widely adopted to enhance charge transport, buffer structural stress, and mitigate structural degradation (Jiang et al., 2025; Yang and Li, 2023). While advanced conductive additives such as graphene (Jeong et al., 2019) and carbon nanotubes (Perez-Gonzalez et al., 2020) are effective, their high cost and complex synthesis limit large-scale application. By comparison, biomass-derived carbon has attracted increasing attention as an alternative electrode material because of its renewability, low cost, and tunable structural characteristics (Gu et al., 2025). Recent studies have shown that biomass-derived carbons can be engineered into porous, doped, and even self-supporting electrode architectures for advanced electrochemical energy-storage systems, highlighting their value beyond that of conventional conductive additives (Huang et al., 2025, 2024). In particular, hydrothermally derived carbon microspheres possess abundant oxygen-containing functional groups, hierarchical porosity, and strong interfacial affinity toward metal species, enabling in situ growth and self-assembly of LDH nanostructures without additional surface modification (Gao et al., 2024; Zhang et al., 2025a).

Bamboo, as a typical lignocellulosic biomass, contains cellulose, hemicellulose, and lignin, which together serve as carbon precursors during hydrothermal carbonization and subsequent carbonization. In the present work, these biomass components do not remain only as native biopolymers in the final electrode; instead, they are converted into bamboo-derived carbon microspheres that provide both the structural carbon framework and surface functionalities for subsequent hydroxide nucleation and growth (He et al., 2025b). Owing to these features, the bamboo-derived carbon microspheres function simultaneously as conductive frameworks and structure-directing platforms, promoting the formation of hierarchical LDH nanoflowers with favorable ion/electron transport pathways. Based on this design, bamboo-derived carbon was introduced to construct a ternary Ni-Co-Mg LDH/carbon composite electrode (NCM@BC) for efficient supercapacitive energy storage. In this system, Mg incorporation helps stabilize the layered framework and regulate growth behavior, while the synergistic Ni-Co redox chemistry ensures high pseudocapacitive activity. As a result, the NCM@BC electrode exhibits excellent electrochemical performance and shows strong potential for application in high-energy asymmetric supercapacitors.

2. Experimental

2.1. Chemicals and materials

Bamboo powder (moso bamboo, passed through a 60-mesh sieve) was used as the biomass precursor. Cobalt(II) nitrate hexahydrate ($Co(NO_3)_2{\cdot}6\,H_2O$, $\geq$ 99%), nickel(II) nitrate hexahydrate ($Ni(NO_3)_2{\cdot}6\,H_2O$, $\geq$ 99%), magnesium sulfate ($MgSO_4$, $\geq$99%), urea ($CO(NH_2)_2$), anhydrous ethanol, polyethylene glycol-600 (PEG-600), potassium hydroxide (KOH), acetylene black, polyvinylidene fluoride (PVDF), and N-methyl-2-pyrrolidone (NMP) were purchased from Shanghai Aladdin Biochemical Technology Co., Ltd. (Shanghai, China). Nickel foam was adopted as the current collector, while Hg/HgO and Pt foil were provided by Kelude Co., Ltd. and used as the reference and counter electrodes.

2.2. Synthesis of NCM@BC electrode materials

2.2.1. Preparation of bamboo-derived carbon (BC)

BC microspheres were produced through a two-step route combining hydrothermal treatment and subsequent carbonization. Briefly, 1 g of bamboo powder was added to 50 mL of deionized water and magnetically stirred to form a homogeneous suspension. The purpose was to ensure uniform contact between the biomass particles and water before hydrothermal treatment rather than to obtain a long-term colloidally stable dispersion. The suspension was then placed in a Teflon-lined stainless-steel autoclave and heated at 220 °C for 12 h. Once cooled to ambient temperature, the resulting solid was recovered by vacuum filtration, repeatedly rinsed with deionized water, and dried at 60 °C. The dried hydrothermal product was then treated in a tubular furnace under N_2 at 800 °C for 1 h (5 °C min-1). After cooling, the carbonized sample was ground and denoted as BC.

2.2.2. Preparation of NCM@BC composite electrode materials

NCM@BC composite electrode materials were prepared by a one-pot solvothermal strategy. $Ni(NO_3)_2{\cdot}6\,H_2O$, $Co(NO_3)_2{\cdot}6\,H_2O$, and $MgSO_4$ were dissolved in 50 mL of an aqueous solution containing 30 vol% ethylene glycol, with a total metal salt amount of 1 mmol and a molar ratio of Ni:Co:Mg = 2:1:2. After the metal salts were completely dissolved by vigorous stirring for 5 min, 1.5 g of urea was added as the

precipitating agent and stirring was continued until a clear solution was obtained. BC was then added in different amounts (10, 20, and 30 mg), followed by continuous stirring for 30 min to form a well-dispersed suspension. The suspension was subsequently placed in a 100 mL Teflon-lined stainless-steel autoclave for solvothermal reaction at 80 °C for 30 h. The solid products were then recovered by centrifugation at 8000 rpm, washed several times with deionized water and ethanol, and dried at 60 °C for 12 h. The resulting products were labeled NCM@BC-10, NCM@BC-20, and NCM@BC-30 according to the BC dosage (Fig. 1).

For comparison, two control samples were also prepared under the same solvothermal conditions. The Mg-free sample was denoted as NC, in which $MgSO_4$ was omitted from the precursor solution. The Mg-containing sample prepared without BC was denoted as NCM. These control samples were used to distinguish the respective roles of Mg incorporation and bamboo-derived carbon introduction.

2.3. Material characterization

FE-SEM (Hitachi S-3400) combined with EDS was used to examine the morphology and elemental distribution of the prepared samples. Their microstructural features were further investigated by HRTEM (JEOL JEM-2100, 200 kV). Phase identification was carried out by X-ray diffraction (XRD) on a PANalytical X'Pert Pro diffractometer with Cu Kα radiation (λ = 1.5406 Å). Surface elemental composition and valence states were analyzed by X-ray photoelectron spectroscopy (XPS, AXIS Ultra). N_2 adsorption-desorption at 77 K were performed on a Micromeritics ASAP 2020 instrument (Huang et al., 2018; Jiang et al., 2025; Zhang et al., 2025a).

2.4. Computational details

Density functional theory (DFT) calculations were performed to clarify the electronic structure and interfacial interaction characteristics of the NCM@BC system. The computational methodology is described in detail in the Supporting Information (SI).

2.5. Electrochemical measurements

Electrochemical tests were conducted on a Zennium electrochemical workstation (Zahner, Germany). The working electrode was fabricated by coating a slurry of active material, acetylene black, and PVDF (8:1:1 by mass) on nickel foam and drying it under vacuum at 80 °C overnight. Measurements were performed in 6 M KOH using a three-electrode (3E) system with Pt foil and Hg/HgO as the counter and reference electrodes, respectively. CV, GCD, and EIS were recorded over 0–0.5 V after 20 activation cycles. The asymmetric supercapacitor was assembled with NCM@BC-20 as the positive electrode. The electrode mass balance and the equations used for device metrics are provided in the SI.

3. Results and discussion

3.1. Morphological and structural properties

The morphology and microstructure of the electrode materials were examined by SEM (Fig. 2a-i). The bamboo-derived carbon (BC) obtained via hydrothermal carbonization followed by high-temperature carbonization exhibits a typical microspherical morphology with relatively smooth surfaces and interconnected structures (Fig. 2a). Although the BC spheres appear morphologically smooth at the SEM scale, hydrothermal carbonization generally preserves abundant oxygen-containing surface functionalities, which can provide effective adsorption and nucleation sites for metal ions during subsequent solvothermal growth. Therefore, the BC microspheres act not only as conductive carbon supports, but also as chemically active substrates for the heterogeneous growth of the layered hydroxide phase (Kumari et al., 2024; Wang et al., 2024). For comparison, the morphology of the NC sample was also characterized. As shown in Fig. S1, NC exhibits an aggregated porous structure without well-defined hierarchical features. However, the pristine NCM sample displays a microspherical morphology composed of densely stacked and interwoven nanosheets (Figs. 2b and 2c), a structural feature commonly observed for multimetal hydroxide materials synthesized under mild solvothermal conditions (Zhang et al., 2024). However, the compact stacking of these nanosheets results in limited internal void space, which may restrict electrolyte penetration and ion transport during electrochemical operation.

Upon the introduction of BC, the resulting NCM@BC composites exhibit markedly different hierarchical architectures, indicating that BC plays a decisive role in regulating the nucleation, growth, and self-assembly behavior of the multimetal layered hydroxide phase. Specifically, the NCM@BC-10 sample (Figs. 2d and 2e) presents a relatively dense three-dimensional network dominated by rod-like or needle-like subunits. Although the presence of BC promotes heterogeneous nucleation, the insufficient BC content leads to excessive aggregation of the active nanostructures, resulting in reduced pore accessibility and limited transport pathways for electrolyte ions and electrons. In contrast, the NCM@BC-20 sample (Figs. 2f and 2g) exhibits a well-defined hierarchical nanoflower-like architecture, in which ultrathin, needle-like NCM nanosheets are uniformly anchored onto the surface of carbon

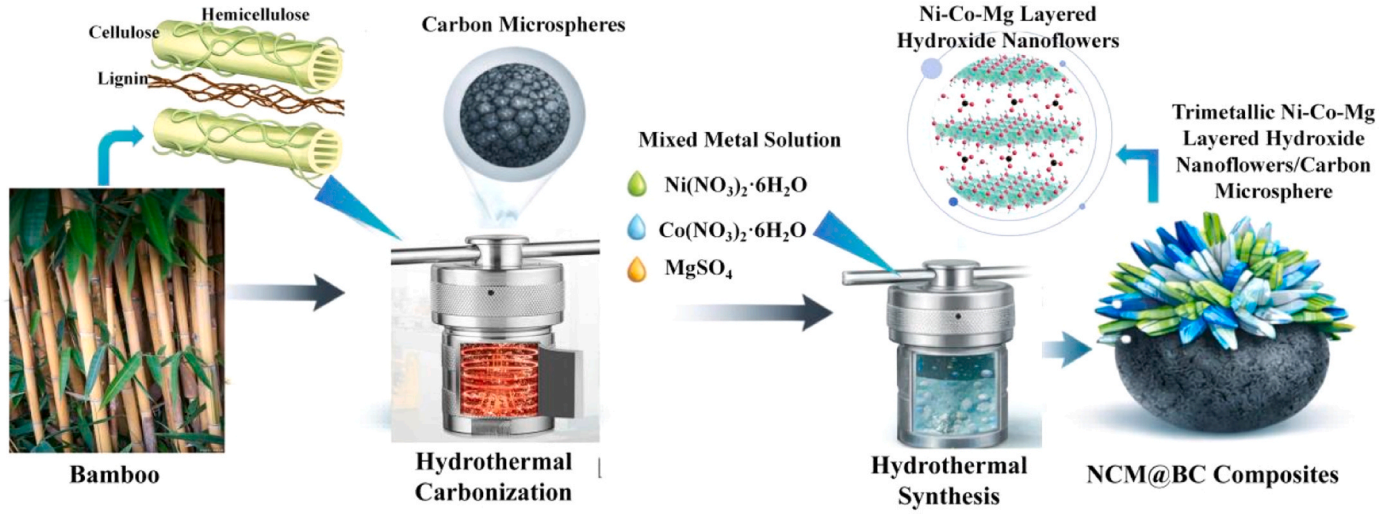

Fig. 1. The synthesis route of NCM@BC composites.

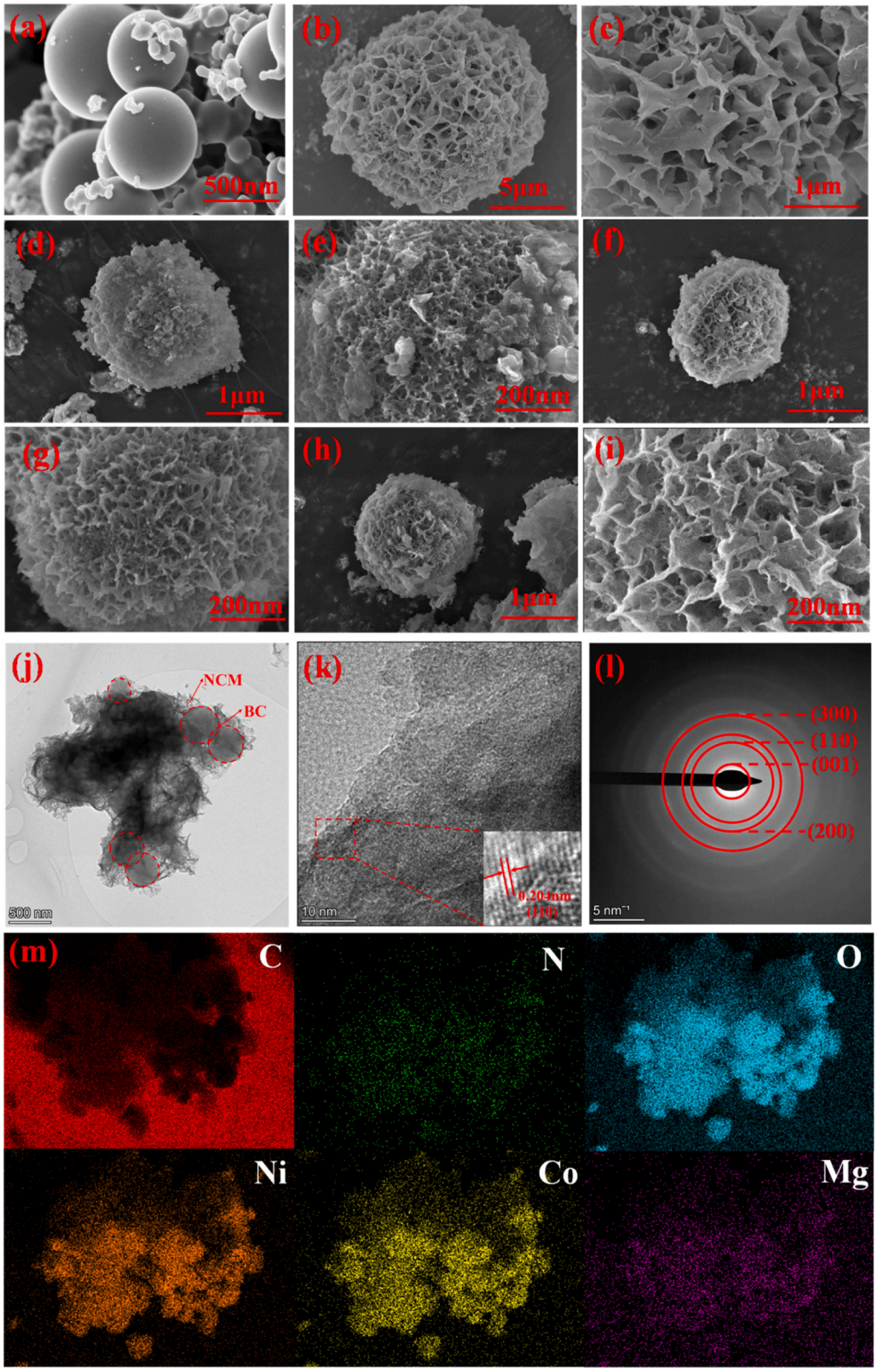

Fig. 2. SEM images of (a) BC, (b–c) pristine NCM, (d–e) NCM@BC-10, (f–g) NCM@BC-20, and (h–i) NCM@BC-30; (j) Low-magnification TEM image of NCM@BC-20 showing BC microsphere domains embedded in the carbon-supported hierarchical assembly; (k) HRTEM image; (l) SAED pattern; and (m) EDS elemental mapping of NCM@BC-20.

microspheres and radially assembled into flower-like spherical assemblies. The open three-dimensional framework with enlarged inter-nanosheet spacing effectively suppresses structural agglomeration, increases the electrochemically accessible surface area, and exposes abundant redox-active sites. Such a hierarchical architecture is highly favorable for rapid electrolyte infiltration and efficient ion/electron transport, which is expected to reduce charge-transfer resistance and enhance both specific capacitance and rate capability (Lan et al., 2024). Moreover, the robust nanoflower-like configuration provides sufficient structural buffering space to accommodate volume variation during repeated Faradaic reactions, thereby contributing to improved cycling stability. When the BC content is further increased to 30 mg, the NCM@BC-30 sample (Fig. 2h,i) undergoes an obvious morphological evolution toward densely stacked nanosheet assemblies. The excessive carbon content disrupts the controlled self-assembly process, leading to a more compact structure with reduced exposed active surface and hindered ion transport pathways, which is detrimental to electrochemical performance.

TEM observation of NCM@BC-20 further clarifies the composite architecture. As shown in Fig. 2j, the particle consists of a carbon-supported hierarchical assembly rather than isolated hydroxide particles. The relatively low-contrast spherical domains can be assigned to the carbon microspheres, while the surrounding high-contrast regions correspond to the attached NCM nanosheets. This morphology is consistent with a carbon-core/LDH-shell-like hierarchical structure formed through heterogeneous nucleation and outward growth of the layered hydroxide phase on the BC surface (Fig. S2). High-resolution TEM analysis (Fig. 2k) reveals distinct lattice fringes within the NCM nanosheets, indicating the presence of locally ordered crystalline domains. The lattice spacing is measured to be approximately 0.20 nm and is assignable to the (110) facet of Ni-Co-based layered hydroxides, implying that the original layered motif is retained in the composite. Notably, the NCM nanosheets are closely attached to the carbon microspheres, forming a carbon-supported hierarchical heterostructure. Such close interfacial contact is beneficial for maintaining structural integrity during cycling and for facilitating electron transport across the LDH/carbon interface. As shown in Fig. 2l, the SAED pattern consists of concentric diffraction rings assignable to the (001), (110), (200), and (300) planes, revealing the polycrystalline character of the sample together with a moderate degree of crystallinity. Such diffraction characteristics are typical of LDH-derived materials synthesized under mild conditions and are advantageous for providing abundant defect sites and electrochemically active surfaces. EDS elemental mapping (Fig. 2m) further shows the co-localization of C, Ni, Co, and Mg signals within the same particle region. This result confirms the homogeneous dispersion of the metal species within the carbon-supported matrix and supports the successful formation of an integrated multicomponent architecture.

The crystalline structure and phase constitution of the samples were examined by XRD, as shown in Fig. 3a. For BC, two broad diffraction bands centered at approximately 22.9° and 43.3° can be assigned to the (002) and (100) planes of disordered carbon, respectively. The broad profiles indicate that the carbon framework is predominantly amorphous, which is typical for hydrothermally derived biomass carbons (Zhou et al., 2020). For pristine NCM and NCM@BC-20, distinct diffraction peaks located at around 11.8°, 33.5°, and 59.7° can be indexed to the (003), (110), and (300) planes of an LDH-type phase

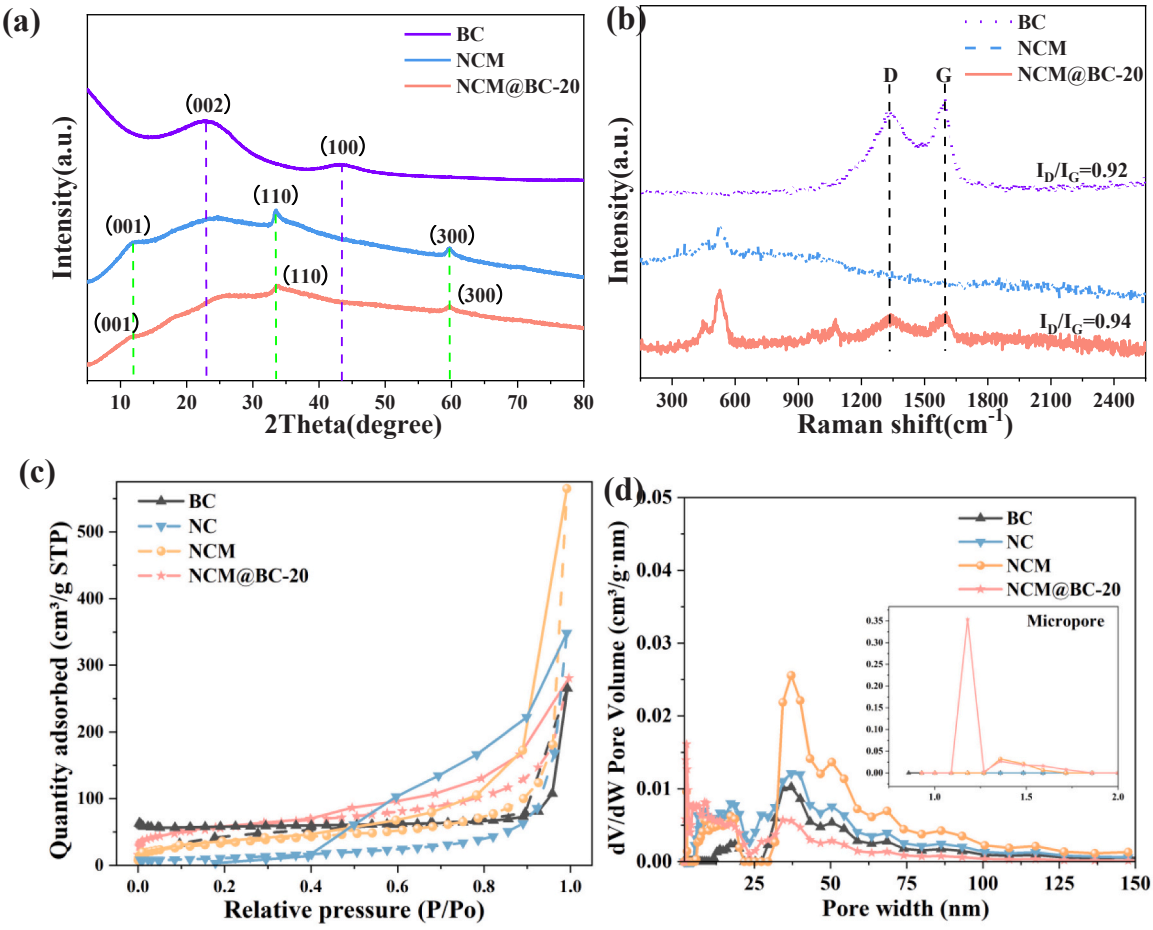

Fig. 3. (a) XRD pattern and (b) Raman spectra; (c) N_2 adsorption/desorption isotherms; (d) PSD curves of BC, NCM, NCM@BC-20 sample in the range of 2–150 nm, the insert is the micropore range less than 2 nm.

(PDF#76–1842). The relatively weak and broadened diffraction features of NCM and NCM@BC-20 indicate that the hydroxide phase retains an LDH-type layered structure but possesses reduced long-range crystallographic ordering, rather than forming a highly crystallized oxide phase. Such broadened reflections are likely associated with nanocrystalline layered domains, imperfect stacking of hydroxide sheets, and the additional structural disorder introduced by Mg incorporation and LDH/carbon interfacial coupling under the mild solvothermal conditions used in this work. Nevertheless, NCM and NCM@BC-20 exhibit closely similar diffraction features, indicating that the incorporation of bamboo-derived carbon preserves the essential layered hydroxide framework. Such partial structural disorder is often beneficial for electrochemical energy storage because it can increase defect-associated active sites and improve their accessibility.

Raman analysis was further conducted to examine the carbon structure and local bonding environment of the composites (Fig. 3b). For both BC and NCM@BC-20, two obvious Raman features appear near 1334 (D bands) and 1588 cm^{-1} (G bands). The former reflects disordered carbon structures, whereas the latter is related to graphitized sp^2 carbon. The calculated I_D/I_G ratios are 0.92 for BC and 0.94 for NCM@BC-20, suggesting a modest increase in defect density in the composite. The slightly higher value for NCM@BC-20 suggests a moderate increase in defect density after coupling with the NCM phase. It should be noted that the Raman response mainly reflects the local structural order of the carbon phase rather than the overall crystallinity of the entire sample. Therefore, the more distinct D/G bands of BC do not imply that BC is more crystalline than NCM in a strict structural sense. In fact, the XRD results indicate that BC remains predominantly disordered carbon, while the crystallinity of NCM should be mainly interpreted from its LDH-related diffraction features (Luo et al., 2022). NCM@BC-20 also shows weak features in the low-wavenumber range (ca. 450–550 cm^{-1}), which are attributable to metal-oxygen vibrational modes from the multimetal hydroxide framework and provide additional evidence for successful coupling between the LDH phase and the carbon matrix.

The N_2 adsorption-desorption isotherms in Fig. 3c and S3 are characteristic of type IV with pronounced H3 hysteresis, suggesting the predominance of mesopores. The PSD curves (Fig. 3d) further show a wide pore distribution extending across the micro-, meso-, and macropore ranges, suggesting the formation of hierarchical porous networks. The quantitative textural parameters are listed in Table S1. The BC sample shows a high S_{BET} (225.38 $m^2\ g^{-1}$) and a dominant micropore contribution ($V_{DR}/V_{0.99} = 0.68$), whereas its mesopore volume remains relatively low. In contrast, the pristine NC sample exhibits a much lower S_{BET} (33.75 $m^2\ g^{-1}$) and a negligible micropore fraction, indicating that densely stacked nanosheets limit the formation of accessible pores and active interfaces. Compared with the Mg-free NC sample, the Mg-containing NCM sample shows obvious increase in specific surface area (119.71 $m^2\ g^{-1}$) and micropore contribution ($V_{DR}/V_{0.99} = 0.19$), indicating that Mg incorporation modifies the crystallization/stacking behavior of the Ni-Co hydroxide framework. This experimental comparison supports the view that Mg primarily acts as a structural modulator rather than as an additional redox-active center within the investigated potential window. Further integration with BC leads to a pronounced optimization of the hierarchical pore structure. Among the composites, NCM@BC-20 exhibits the most balanced textural characteristics, featuring a relatively high S_{BET} (193.26 $m^2\ g^{-1}$), an enhanced V_{DR} (0.079 $cm^2\ g^{-1}$), and a reduced average pore size (5.94 nm). Such a hierarchical pore network, in which micropores provide abundant electrochemically active interfaces while mesopores act as ion-buffering reservoirs and fast diffusion pathways, is highly favorable for efficient electrolyte penetration and rapid OH^- transport. These structural advantages are consistent with the reduced charge-transfer resistance and superior rate capability observed for NCM@BC-20 in electrochemical measurements. By comparison, insufficient BC loading fails to effectively suppress nanosheet aggregation, while excessive BC incorporation leads to a reduced micropore fraction and less efficient utilization of redox-active sites. Overall, the optimized hierarchical pore structure of NCM@BC-20 provides a solid structural foundation for its enhanced electrochemical performance.

3.2. Chemical characteristics

To further elucidate the surface chemical states, interfacial bonding environment, and the role of Mg incorporation in the composite electrodes, XPS and DFT calculations were employed. The XPS survey spectra of BC, NCM, and NCM@BC-20 are presented in Fig. 4a. Distinct signals corresponding to C, N, O, Ni, Co, and Mg are clearly detected for NCM@BC-20, confirming the successful integration of the multimetal layered hydroxide with the bamboo-derived carbon framework. Compared with pristine NCM, the NCM@BC-20 composite exhibits an increased carbon and oxygen content (Table S2), reflecting the incorporation of oxygen-rich biomass-derived carbon and the formation of an extended interfacial contact area.

As shown in Fig. 4b and Table S3, the C 1 s spectrum is resolved into four peaks at 284.8, 286.1, 287.0, and 288.6 eV, corresponding to C-C/C═C, C-O, C═O, and O-C═O species, respectively. These oxygenated surface functionalities inherited from bamboo-derived carbon facilitate the nucleation of the NCM phase and promote tight interfacial coupling with the layered hydroxide framework. Importantly, the persistence of these functional groups in NCM@BC-20 suggests that the carbon scaffold not only serves as a conductive network but also actively participates in interfacial chemical regulation (Zhao et al., 2025).

The O 1 s spectra (Fig. 4c and Table S4) further reveal the chemical environment of oxygen species. For BC, the peaks at 530.6, 532.1, and 533.8 eV correspond to C═O, C–OH/C–O–C, and –COOH groups, respectively. These oxygen-containing groups are important because they provide coordination/adsorption sites for the precursor metal ions, thereby favoring heterogeneous nucleation and stabilizing the attachment of the hydroxide phase on the BC surface. In contrast, NCM and NCM@BC-20 display characteristic contributions from metal–oxygen bonds (530.2 eV), hydroxyl groups (531.1 eV), and adsorbed oxygen species (532.9 eV), indicative of a typical LDH-like chemical environment. A high proportion of hydroxyl-associated oxygen species can facilitate fast and reversible surface Faradaic reactions under alkaline conditions (Luo et al., 2021a). The N 1 s spectra (Fig. S4 and Table S5) of BC, NCM, and NCM@BC-20 exhibit contributions from pyridinic N, pyrrolic N, and oxidized nitrogen species. These nitrogen functionalities enhance surface polarity and electronic conductivity, thereby facilitating electrolyte infiltration and interfacial charge transfer (Zhang et al., 2024).

As shown in Figs. 4d and 4e, the Ni 2p and Co 2p spectra reveal that NCM@BC-20 contains Ni^{2+} as well as Co species with mixed Co^{2+}/Co^{3+} valence states (Table S6, S7). Such mixed-valence states provide abundant redox-active centers and underpin the pseudocapacitive charge storage behavior. In addition, clear Mg 1 s and Mg 2p signals (Fig. 4f) confirm that Mg is incorporated as a stable divalent species. Although Mg^{2+} is electrochemically inactive within the applied potential window, its presence is expected to regulate local coordination environments and stabilize the layered framework rather than directly participating in Faradaic reactions.

To gain atomistic insights into the roles of Mg incorporation and carbon coupling, DFT calculations were performed. As shown in Fig. 5a and b, Mg can be stably introduced into the Ni-Co LDH lattice (NC), and the calculated substitution formation energy is 0.41 eV, indicating that Mg incorporation is thermodynamically feasible. This result is consistent with the experimentally observed homogeneous Mg distribution. The moderate formation energy further suggests that Mg can be incorporated into the layered hydroxide framework without causing pronounced lattice instability and thus primarily acts as a structural modulator. The optimized LDH/carbon interface models are shown in Fig. 5c and d. The Ni-Co-Mg LDH/carbon interface exhibits a more negative binding

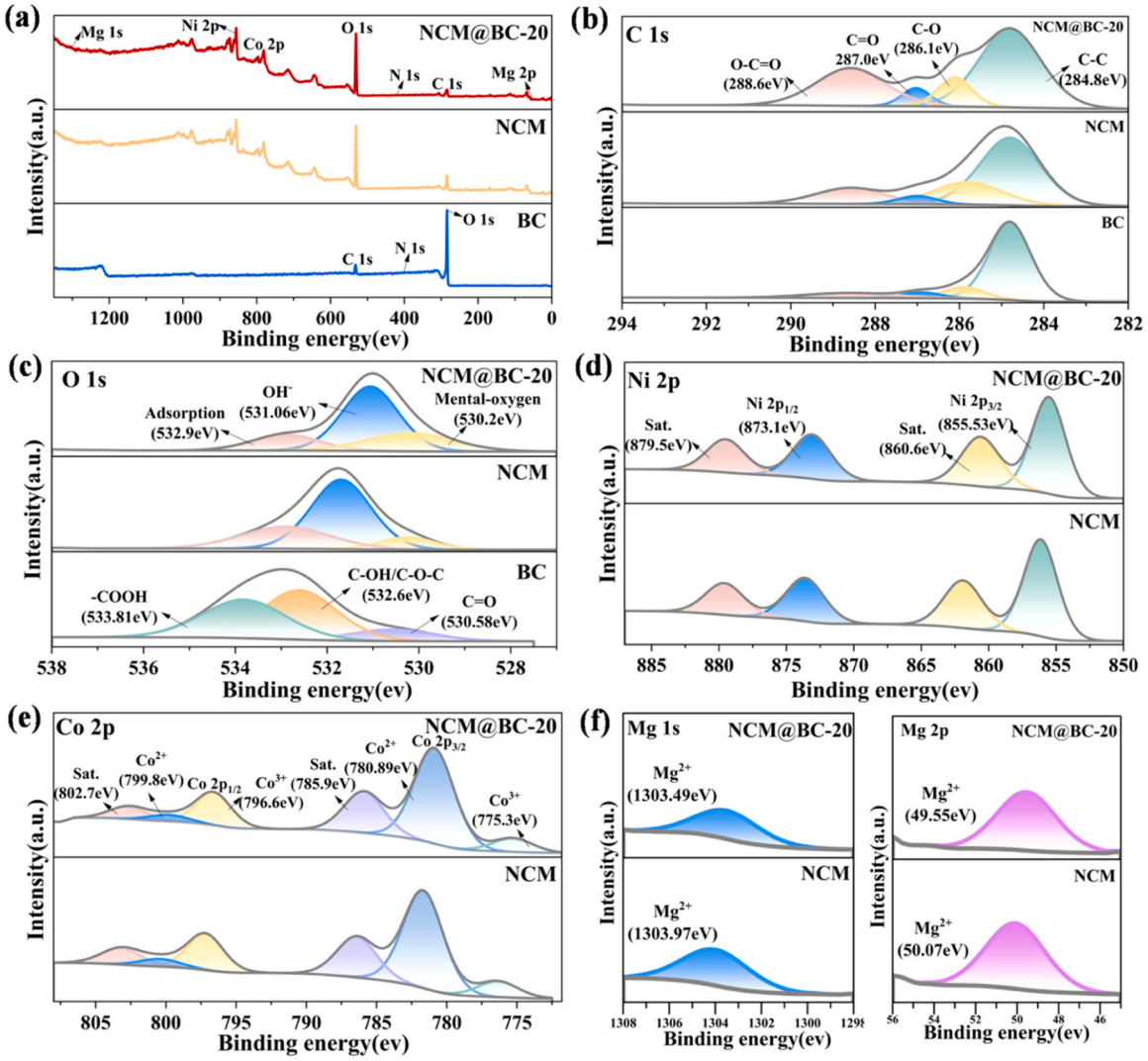

Fig. 4. XPS spectra of BC, NCM, and NCM@BC-20, including (a) full survey spectra, (b) C 1 s, (c) O 1 s high-resolution spectra, together with (d) Ni 2p, (e) Co 2p, and (f) Mg 1 s, 2p high-resolution spectra of NCM@BC-20.

energy (NCM@BC, –2.71 eV) than the Mg-free Ni–Co LDH/carbon interface (NC@BC, –2.18 eV), indicating that Mg incorporation strengthens the interaction between the hydroxide phase and the carbon substrate. Charge-density-difference analysis further clarifies the nature of this interface. As shown in Fig. 5e, localized charge accumulation and depletion are observed near the NCM@BC contact region, demonstrating clear interfacial charge redistribution rather than simple physical contact. Such interfacial electronic polarization is beneficial for stabilizing the heterointerface and facilitating charge transfer across the composite structure. Considering the alkaline electrolyte environment, K^+ adsorption was used as a representative descriptor to evaluate ion affinity. As shown in Fig. 5f and Fig. S5, the adsorption energy becomes progressively more negative from pristine LDH (NC, –2.02 eV) to Mg-incorporated LDH (NCM, –2.39 eV) and further to the LDH/carbon heterostructure (NCM@BC-20, –3.19 eV), indicating increasingly favorable ion–surface interaction after Mg regulation and carbon coupling. This enhanced ion affinity provides a reasonable theoretical explanation for the experimentally observed improvements in pseudocapacitive contribution, rate capability, and cycling stability. Overall, the combined XPS and DFT results indicate that Mg incorporation stabilizes the layered hydroxide framework and strengthens the NCM@BC interface without altering the intrinsic redox roles of Ni and Co. The optimized local electronic environment, interfacial charge redistribution, and enhanced ion adsorption together account for the superior electrochemical performance of the NCM@BC composite.

3.3. *Electrochemical performance*

The electrochemical behavior was systematically evaluated in a 3E system. The CV curves of BC at scan rates from 5 to 200 mV s^{-1} are presented in Fig. 6a. The curves display a nearly rectangular shape with slight deviation, suggesting that charge storage is dominated by EDLC, accompanied by a limited pseudocapacitive contribution from surface oxygen- and nitrogen-containing groups (Wang et al., 2025b). Even at high scan rates, the overall profile remains largely unchanged, indicating rapid ion adsorption/desorption and good rate response (Zhao et al., 2025). In Fig. 6b, the GCD profiles of BC show nearly symmetric triangular shapes over 0.5–10 A g^{-1}, characteristic of a highly reversible capacitive process.

By contrast, the CV curves of NC, pristine NCM, and the NCM@BC composites collected at 5 mV s^{-1} within −0.1–0.55 V (Fig. 6c) exhibit obvious redox peaks, indicating that Faradaic reactions dominate the charge-storage process in these NCM-based electrodes (Luo et al., 2021b). These redox features are associated with the reversible valence transitions of Ni and Co species in alkaline electrolyte and can be described by the following reactions:

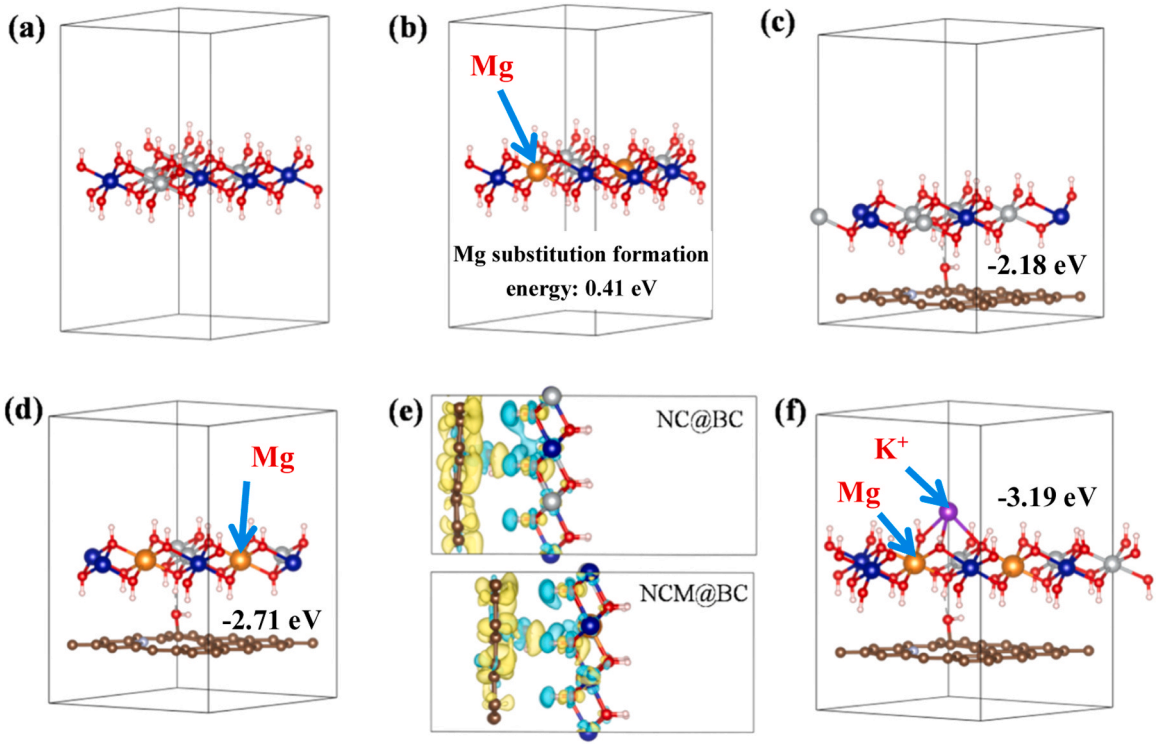

Fig. 5. (a) Optimized atomic structure of pristine NC sample; (b) optimized atomic structure of Mg-incorporated NCM sample, with the Mg substitution site indicated; (c) optimized NC/BC interfacial structure and corresponding binding energy; (d) optimized NCM/BC interfacial structure and corresponding binding energy; (e) charge-density-difference maps at the LDH/carbon interface (yellow: electron accumulation; cyan: electron depletion); and (f) optimized K^+ adsorption configuration on the NCM/BC heterostructure. The comparative K^+ adsorption energies for pristine NC, NCM, and NCM/BC heterostructures are provided in Fig. S5.

$$Ni(OH)_2 + OH^- \leftrightarrow NiOOH + H_2O + e^-$$

$$Co(OH)_2 + OH^- \leftrightarrow CoOOH + H_2O + e^-$$

$$CoOOH + OH^- \leftrightarrow CoO_2 + H_2O + e^-$$

In comparison with NC and pristine NCM, all NCM@BC electrodes deliver more pronounced redox responses and broader CV areas, indicating more effective participation of active sites in the charge-storage process and enhanced pseudocapacitive behavior. This improvement can be ascribed to the combined effect of Mg-induced electronic modulation and the intimate coupling between the LDH phase and BC, which together improve the accessibility of surface-active sites and facilitate interfacial redox reactions. Among the composite electrodes, NCM@BC-20 shows the largest enclosed CV area, implying the highest charge-storage capability. When the BC content is further increased to 30 mg, the electrochemical response declines, likely because excessive carbon addition induces partial aggregation and hampers efficient ion transport (Wang et al., 2025b).

The CV curves of NCM@BC-20 at different scan rates are displayed in Fig. 6d. With increasing scan rate, the peak currents increase continuously while the overall curve shape is largely maintained, revealing favorable reaction kinetics and good rate tolerance. The gradual shift of the anodic and cathodic peaks at higher scan rates is attributable to electrode polarization, a common feature of pseudocapacitive materials (Chen et al., 2025; He et al., 2025a; Yang and Li, 2023).

Further evidence is provided by the GCD results. As shown in Fig. 6e, NC, pristine NCM, and NCM@BC all exhibit discharge profiles with distinct voltage plateaus, confirming the Faradaic nature of the charge-storage process (Luo et al., 2022). The specific capacitances of NCM@BC-10, NCM@BC-20, and NCM@BC-30 are calculated to be 1118, 1226.8, and 1198.4 F g^{-1}, respectively. NCM@BC-20 delivers the highest value, markedly exceeding those of pristine NCM (931.8 F g^{-1}) and NC (670 F g^{-1}). It should be noted that the capacitance values were calculated based on the total mass of the composite active material. Although BC itself exhibits a relatively low capacitance and mainly contributes electric double-layer charge storage, its incorporation is still beneficial because it provides conductive pathways, nucleation/anchoring sites for hydroxide growth, and an optimized hierarchical pore structure. Therefore, the improved performance of NCM@BC-20 originates from the synergistic integration of BC with the NCM phase (Gao et al., 2024). DFT results further support this interpretation by showing stronger interfacial binding and enhanced K^+ adsorption at the Mg-regulated LDH/carbon interface, both of which are favorable for fast redox reactions and efficient charge storage.

The GCD curves of NCM@BC-20 at different current densities are shown in Fig. 6f. The corresponding specific capacitances remain at 1226.8, 1130.4, 993.0, and 886.0 F g^{-1} at 1, 2, 5, and 10 A g^{-1}, respectively, demonstrating excellent rate performance. The decrease in capacitance at high current density is mainly associated with insufficient ion diffusion into the inner active regions under rapid charge-discharge conditions. Even so, the capacitance retention remains high, highlighting the role of BC in promoting efficient electron/ion transport throughout the composite (Zhang et al., 2025a).

To further probe the kinetic characteristics, EIS measurements were carried out (Fig. 6g and Table S8). All electrodes show small solution resistance values (Rs≈0.5 Ω), indicating good electrical contact and low ohmic loss. Notably, NCM@BC-20 presents the most reduced semicircle in the high-frequency region, suggesting the most favorable interfacial charge-transfer kinetics. This result points to faster interfacial electron transport and improved reaction kinetics (Zhao et al., 2025). Such behavior is consistent with the DFT results, which indicate that Mg incorporation enhances electronic coupling at the LDH/carbon interface and promotes interfacial charge redistribution, thereby lowering the kinetic barrier for charge transfer. The rate capability comparison is summarized in Fig. 6h. At 10 A g^{-1}, NCM@BC-20 retains 70.6% of its

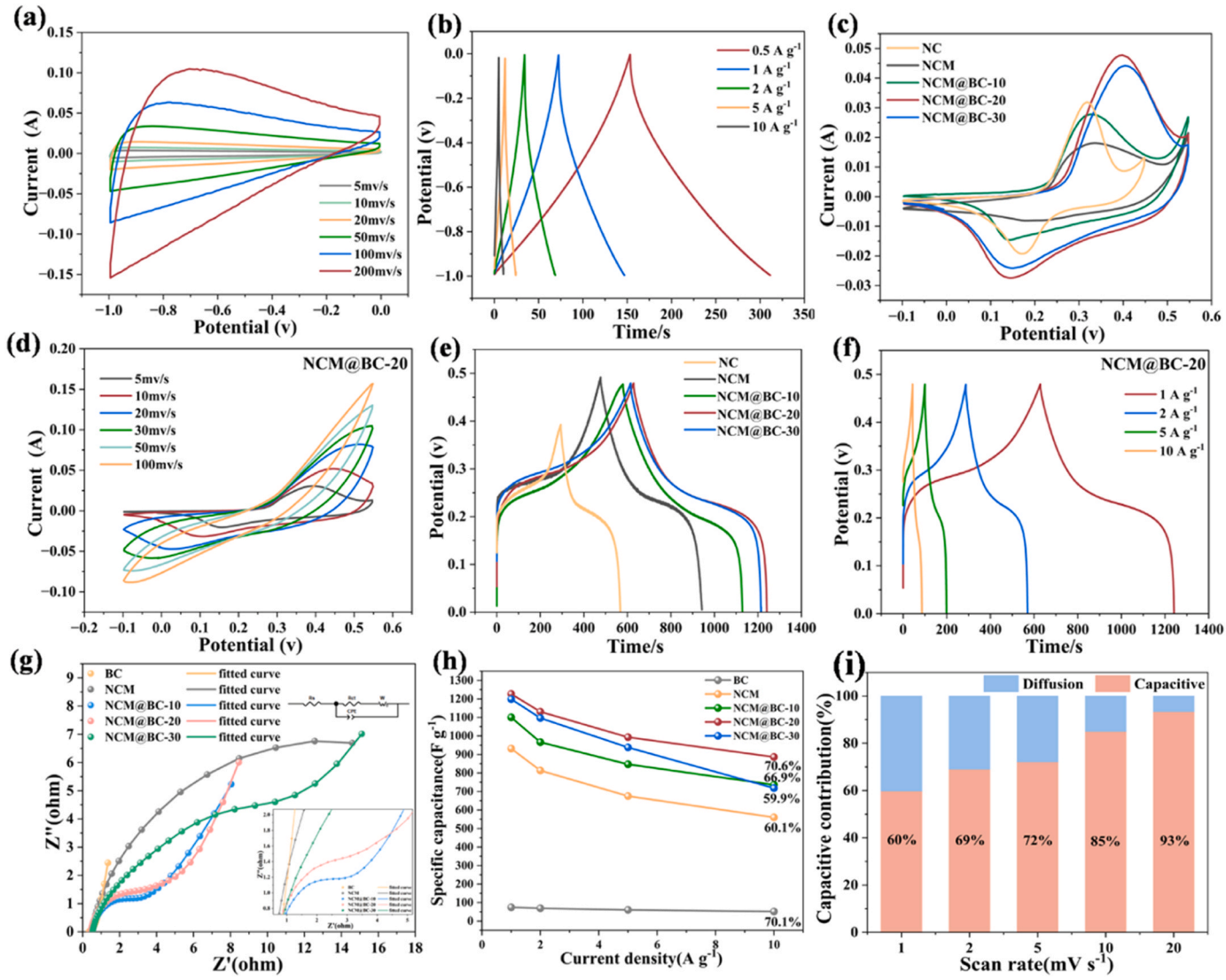

Fig. 6. Electrochemical responses of BC, NC, pristine NCM, and NCM@BC electrodes: (a) CV behavior of BC at different scan rates; (b) GCD behavior of BC at various current densities; (c) CV curves of NC, pristine NCM, and NCM@BC electrodes obtained at 5 mV s^{-1}; (d) scan-rate-dependent CV curves of NCM@BC-20; (e) GCD curves of NC, pristine NCM, and NCM@BC electrodes recorded at 1 A g^{-1}; (f) current-density-dependent GCD curves of NCM@BC-20; (g) Nyquist spectra of BC, NCM, and NCM@BC electrodes from EIS analysis, with the equivalent circuit shown in the inset; (h) rate capability comparison among the different electrodes; (i) deconvolution of capacitive and diffusion-controlled charge-storage contributions for NCM@BC-20 at different scan rates.

initial capacitance, which is clearly higher than that of pristine NCM (60.1%) and NCM@BC-30 (59.9%). This result demonstrates that an appropriate BC content is essential for maintaining structural integrity and sustaining rapid ion/electron transport under high-rate operation. The improved high-rate response is also in line with the DFT analysis, which suggests strengthened interfacial coupling and more favorable charge redistribution after Mg regulation.

The charge-storage mechanism of NCM@BC-20 was further examined by fitting the CV response with the power-law equation $i = av^b$ (Luo et al., 2022; Wang et al., 2025b). The obtained b values are 0.72 and 0.59 for the anodic and cathodic peaks, respectively, indicating a mixed kinetic behavior involving both surface-controlled and diffusion-controlled processes, while the cathodic process exhibits a more pronounced diffusion constraint (Fig. S6). The relative contributions were further quantified by Dunn's method. As shown in Fig. 6i, the surface-controlled contribution increases from 60% at 1 mV s^{-1} to 93% at 20 mV s^{-1}, indicating that capacitive processes become increasingly dominant at higher scan rates. This behavior can be attributed to the hierarchical pore structure and strong LDH-carbon interfacial coupling, both of which favor rapid surface redox reactions and efficient charge transport.

3.4. Electrochemical properties of the ASC devices

The device-level performance of NCM@BC was further investigated by assembling an asymmetric supercapacitor with NCM@BC-20 as the cathode and biomass-derived porous activated carbon (AC) from our earlier work (Luo et al., 2022) as the anode. The working voltage of the device was first determined from the electrochemical stability of the two electrodes. As presented in Fig. 7a, when the cell voltage was increased stepwise from 1.0 to 1.6 V at 10 mV s^{-1}, the CV profiles remained well preserved without obvious deformation, indicating stable and reversible operation within this range. Further extension of the voltage window led to noticeable polarization and deviation from the original curve shape, implying the occurrence of side reactions (Zhang et al., 2024). To further confirm the suitable operating voltage, GCD curves were recorded at 1 A g^{-1} under different voltage windows (Fig. 7b). The results are consistent with the CV analysis and support the selection of 1.6 V as the

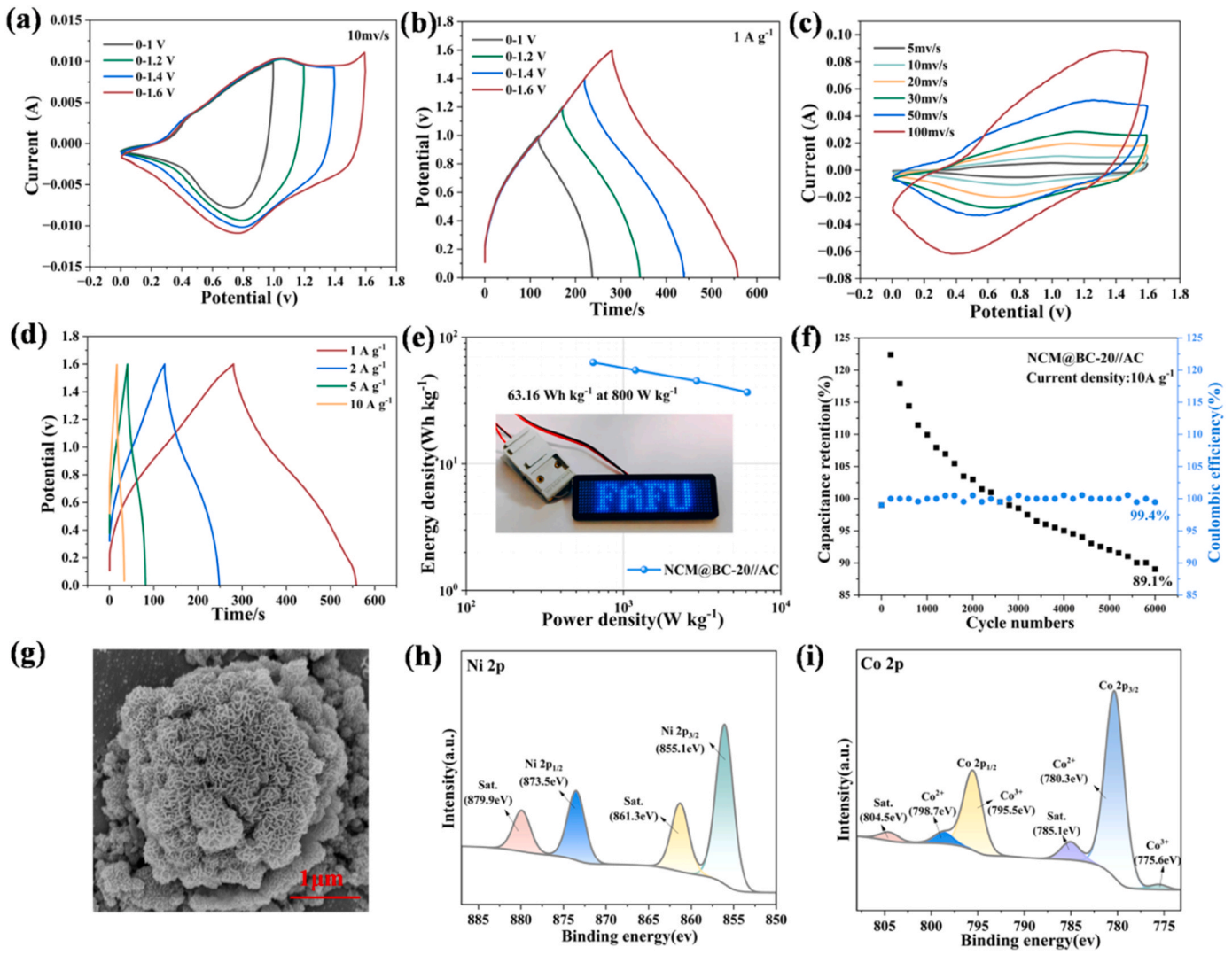

Fig. 7. Electrochemical responses of the NCM@BC-20//AC asymmetric supercapacitor: (a) CV behavior at 10 mV s^{-1} over different cell-voltage windows; (b) GCD profiles at 1 A g^{-1} under different voltage windows; (c) scan-rate-dependent CV curves; (d) current-density-dependent GCD curves; (e) Ragone plot with an inset photograph of an LED lit by the assembled device; (f) long-term cycling performance and coulombic efficiency at 10 A g^{-1}; (g) SEM images of the NCM@BC-20 positive electrode before and after 6000 charge-discharge cycles at 10 A g^{-1} in the asymmetric supercapacitor device; and (h-i) Ni 2p and Co 2p high-resolution XPS spectra of the cycled NCM@BC-20 positive electrode after 6000 charge-discharge cycles.

working voltage for subsequent device evaluations.

After the voltage window was established, the rate-dependent electrochemical behavior of the assembled device was evaluated. The CV profiles in Fig. 7c remain largely unchanged over the scan-rate range of 5–100 mV s^{-1}, suggesting fast electrochemical response and stable rate performance for the device. The GCD curves at different current densities are shown in Fig. 7d. All profiles are nearly symmetric, with weak plateau features, indicating good reversibility and a charge-storage mechanism involving both capacitive and Faradaic contributions (Zhao et al., 2025; Zhang et al., 2025a; Wang et al., 2025b). The very small IR drop at the initial stage of discharge suggests low internal resistance, which can be related to the conductive BC framework and the effective matching between the positive and negative electrodes. Based on the GCD results, the device delivers specific capacitances of 173.6, 154.5, 126.9, and 103.1 F g^{-1} at 1, 2, 5, and 10 A g^{-1}, respectively. At elevated current densities, the reduced capacitance is primarily caused by insufficient ion diffusion and limited access to active sites under fast charging-discharging conditions, which is a common feature of hybrid supercapacitors (Zhang et al., 2024; Wang et al., 2023b; Yang and Li, 2023).

As indicated by the Ragone plot in Fig. 7e, the NCM@BC-20//AC device achieves 63.16 Wh kg^{-1} at a power density of 800 W kg^{-1}. Even under higher-power operation, the device still shows competitive energy density compared with many previously reported biomass-based and multimetal asymmetric supercapacitors (Table 1). This performance can be attributed to the cooperative effect between the multimetal LDH-derived active phase and the conductive porous carbon scaffold. In particular, Mg incorporation helps optimize electronic interaction within the Ni-Co hydroxide framework and strengthens charge transfer across the LDH/carbon interface, while the porous BC matrix provides continuous electron-transport pathways and relieves structural stress during repeated Faradaic reactions (Zhao et al., 2025; Tang et al., 2022; Gao et al., 2024).

Long-term cycling performance was examined at 10 A g^{-1} (Fig. 7f). The capacitance shows an initial activation-induced increase during the early cycles, followed by gradual stabilization, which can be ascribed to improved electrolyte infiltration, progressive exposure of electroactive sites, and reversible surface reconstruction of the LDH phase in alkaline medium. After the activation stage, the device retains 89.1% of its peak capacitance after 6000 cycles, together with a coulombic efficiency of 99.4%, indicating good reversibility and acceptable structural durability. Although this cycling performance is competitive, the gradual

Table 1
Comparison of the electrochemical properties of previously reported ASCs.

Material	Energy density (Wh kg^{-1})	Power density (W kg^{-1})	Cyclic stability (% after cycle)	Ref.
MNCO//AC	31.5	393	95 after 4000	(Hussain et al., 2021)
NCBS/C //AC	53	850	83.8 after 5000	(Liu et al., 2022)
NiCoP/HMCS-2//AC	56.4	799.92	91.2 after 5000	(Liu et al., 2024a)
NiCoLDH@LHC $_{90}$ //LHC	35.4	200.01	93.7 after 10000	(Liu et al., 2024b)
NCNRs@NCNSs//AC	22.8	375	90.9 after 5000	(Wan et al., 2015)
CS NTs@NC LDH NSs//AC ASC	50	839	86.4 after 5000	(Jia et al., 2018)
CoWO4/CoNiFe-LDH-0.50//AC	40.5	775	70.3 after 10000	(Zhang et al., 2025b)
NCM@BC-20// AC	63.2	800	89.1 after 6000	This work

capacitance decay suggests that some structural/electrochemical evolution still occurs during prolonged operation. Considering that the positive electrode stores charge through repeated Faradaic reactions while the activated carbon negative electrode mainly contributes electric double-layer capacitance, the observed fading is more likely associated with the progressive surface evolution of the LDH-based positive electrode. Post-cycling characterization further supports this interpretation. As shown in Fig. 7g, the cycled positive electrode largely preserves its hierarchical morphology after prolonged cycling, although slight surface coarsening and partial densification of the outer subunits can be observed. In addition, the post-cycling XPS spectra (Fig. 7h-i and Fig. S7) indicate that the electrode still retains characteristic C, O, Ni, and Co signals, together with typical Ni/Co-based hydroxide/oxyhydroxide chemical features. The O 1 s spectrum still shows metal-oxygen, hydroxyl-related oxygen, and adsorbed oxygen components (Fig. S7), while the Ni 2p and Co 2p spectra confirm the persistence of electrochemically relevant Ni/Co surface species after long-term cycling (Fig. 7h-i). These results suggest that the BC-supported hierarchical architecture helps maintain structural continuity and effective electron/ion transport pathways during cycling, while gradual surface chemical evolution of the LDH phase likely contributes to the moderate capacitance decay (Xie et al., 2018; Yin et al., 2019). In addition, the inset photograph in Fig. 7e shows that a single assembled device can directly light a commercial LED, visually demonstrating its practical output capability. Overall, the results confirm that integrating multimetal LDH chemistry with biomass-derived carbon engineering is an effective strategy for constructing high-performance and sustainable asymmetric supercapacitors.

4. Conclusion

A self-assembly route mediated by bamboo-derived carbon was established to fabricate Ni-Co-Mg layered hydroxide/carbon composites with a hierarchical flower-like architecture. In this system, the bamboo-derived carbon microspheres served simultaneously as conductive scaffolds and nucleation platforms for the growth of hydroxide nanosheets, thereby promoting the formation of an open electrode structure favorable for electrolyte penetration and charge transport. Meanwhile, Mg incorporation contributed to stabilizing the layered hydroxide framework and modulating the local electronic structure, rather than directly participating as an electroactive redox species. The optimized NCM@BC-20 electrode achieves 1226.8 F g^{-1} at 1 A g^{-1} and shows good rate capability as a result of the synergistic structural and compositional effects. Moreover, the assembled asymmetric supercapacitor operated stably over a voltage window of 1.6 V, delivered an energy density of 63.16 Wh kg^{-1} at a power density of 800 W kg^{-1}, and preserved 89.1% of its maximum capacitance after 6000 cycles. More importantly, this study highlights the feasibility of converting bamboo biomass into a functional carbon component that can direct heterostructure construction and enhance electrochemical performance, offering a viable strategy for the high-value utilization of bamboo resources in advanced energy-storage applications. Future work may focus on the controllable regulation of bamboo-derived carbon microstructure, optimization of Mg content, and direct characterization of interfacial evolution during long-term cycling to further improve the stability and practical applicability of such biomass-derived heterostructure electrodes.

CRediT authorship contribution statement

Zhiying Lin: Software, Investigation. **Qianqian Zhang:** Writing – original draft, Resources, Methodology, Data curation, Conceptualization. **Lu Luo:** Software, Investigation, Data curation. **Qingcai Cai:** Software, Resources. **Jiuping Rao:** Supervision, Resources, Data curation. **Jiawei Qiang:** Resources, Methodology. **Weigang Zhao:** Writing – review & editing, Writing – original draft, Supervision, Project administration, Investigation, Data curation, Conceptualization. **Mizi Fan:** Writing – review & editing, Supervision, Conceptualization. **Qinzhi Zeng:** Writing – review & editing, Investigation, Funding acquisition, Conceptualization. **Menghan Li:** Writing – original draft, Software, Methodology, Data curation, Conceptualization.

Declaration of Competing Interest

The authors declare that they have no known competing financial interests or personal relationships that could have appeared to influence the work reported in this paper.

Acknowledgement

We gratefully acknowledge the support by the Zhenghe Rural Revitalization Research Institute of Fujian Agriculture and Forestry University. The authors extend their gratitude from Scientific Compass (www.shiyanjia.com) for providing invaluable assistance with the XPS analysis.

Appendix A. Supporting information

Supplementary data associated with this article can be found in the online version at doi:10.1016/j.indcrop.2026.123404.

Data availability

Data will be made available on request.

References

Braff, W.A., Mueller, J.M., Trancik, J.E., 2016. Value of storage technologies for wind and solar energy. Nat. Clim. Change 6 (10), 964–969.
Chen, F., Chen, C., Hu, Q., Xiang, B., Song, T., Zou, X., Li, W., Xiong, B., Deng, M., 2020. Synthesis of CuO@CoNi LDH on Cu foam for high-performance supercapacitors. Chem. Eng. J. 401, 126145.
Chen, F., Li, J., Shao, Y., Zhu, Z., Shen, T., Chen, K., Chen, Y., Chen, Y., 2025. ZIF-67 wraps Ni-Mn LDHs nanosheets to enhance the capacitive contribution of supercapacitors. Chem. Eng. J. 507, 160454.
Cheng, S., Zhang, Y., Liu, Y., Sun, Z., Cui, P., Zhang, J., Hua, X., Su, Q., Fu, J., Xie, E., 2021. Energizing Fe2O3-based supercapacitors with tunable surface pseudocapacitance via physical spatial-confining strategy. Chem. Eng. J. 406, 126875.
Gao, J., Wang, Z.Q., Wang, Z.F., Li, B., Liu, Z.Y., Huang, J.J., Fang, Y.T., Chen, C.M., 2024. Biomass-based controllable morphology of carbon microspheres with multi-layer hollow structure for superior performance in supercapacitors. J. Colloid Interface Sci. 658, 90–99.
Gu, J., Jia, Z., Wang, B., Chang, Z., Xu, X., Liu, H., Liao, J., Zhai, S., Zhang, F., Huang, L., 2025. Hemicellulose-derived carbonaceous coated-carbon cloth as self-standing

electrode materials for a zinc ion capacitor. ACS Sustain. Chem. Eng. 13 (50), 21825–21833.
Guerra, O.J., Zhang, J., Eichman, J., Denholm, P., Kurtz, J., Hodge, B.M., 2020. The value of seasonal energy storage technologies for the integration of wind and solar power. Energy &amp Environ. Sci. 13 (7), 1909–1922.
He, L., Cai, P., Lai, H., Lu, K., Xu, Z., Zeng, R., Hao, C., Wang, Z., Gan, W., 2025a. Sandwich-like NiFe-LDH/MnCO3/MXene ternary nanocomposites serve as battery-type electrode for high-performance asymmetric supercapacitor. Chem. Eng. J. 504, 159149.
He, X.X., Li, L., Wu, X., Chou, S.L., 2025b. Sustainable hard carbon for sodium-ion batteries: precursor design and scalable production roadmaps. Adv. Mater. 37 (36), e2506066.
Huang, L., Gu, Z., Gu, J., Zhang, F., Zhuang, J., Ma, Q., Zhang, T., Li, J., Liu, H., Feng, W., 2024. Green synthesis of sodium pyrithione salt-activated biomass-derived carbon for aqueous zinc-ion capacitors. Green. Chem. 26 (19), 10196–10204.
Huang, L., Gu, J., Wang, B., He, W., Xiao, S., Liao, J., Chang, Z., Jia, Z., Zhai, S., He, Y., Liu, H., Zhang, F., Feng, W., 2025. Surface pyrolysis towards graphite heterojunctions for aqueous Zinc-ion capacitor. Chem. Eng. J. 513, 163094.
Huang, L., Liu, B., Hou, H., Wu, L., Zhu, X., Hu, J., Yang, J., 2018. Facile preparation of flower-like NiMn layered double hydroxide/reduced graphene oxide microsphere composite for high-performance asymmetric supercapacitors. J. Alloy. Compd. 730, 71–80.
Hussain, I., Lamiel, C., Qin, N., Gu, S., Li, Y., Wu, S., Huang, X., Zhang, K., 2021. Development of vertically aligned trimetallic Mg-Ni-Co oxide grass-like nanostructure for high-performance energy storage applications. J. Colloid Interface Sci. 582, 782–792.
Jeong, J.H., Lee, G.W., Kim, Y.H., Choi, Y.J., Kim, K.B., 2019. A holey graphene-based hybrid supercapacitor. Chem. Eng. J. 378, 122126.
Jia, H., Wang, Z., Zheng, X., Lin, J., Liang, H., Cai, Y., Qi, J., Cao, J., Feng, J., Fei, W., 2018. Interlaced Ni-Co LDH nanosheets wrapped Co9S8 nanotube with hierarchical structure toward high performance supercapacitors. Chem. Eng. J. 351, 348–355.
Jiang, J., Luo, Y., Wang, X., Liu, Z., Cui, S., Cheng, L., Li, Z., Jiao, Z., 2025. Synergistic engineering of structure and interface in NiMn-LDH on hollow graphene spheres for high-performance flexible supercapacitors. J. Alloy. Compd. 1048, 185146.
Kumar, S., Saeed, G., Zhu, L., Hui, K.N., Kim, N.H., Lee, J.H., 2021. 0D to 3D carbon-based networks combined with pseudocapacitive electrode material for high energy density supercapacitor: a review. Chem. Eng. J. 403, 126352.
Kumari, K., Joy, A., Saren, P., Acharya, S., Nayak, G.C., 2024. Synthesis of highly porous hybrid nanocomposite of hemp derived carbon nanosheet/carbon nanotube/manganese cobalt oxide for asymmetric supercapacitor. Mater. Chem. Phys. 313, 128677.
Lan, Y., Yu, R., Wang, Q., Dai, J., 2024. Synthesis of ultra-high specific surface area trimetallic NiCoMg-LDH hollow cage via bimetallic ion etching for hybrid supercapacitors. Ionics 30 (5), 3033–3044.
Liu, S., Fan, J., Ren, L., Shi, Q., Wang, Y., Guo, J., Tong, J., 2024a. Nickel–cobalt bimetallic phosphide/hollow-structured carbon nanosphere composites for supercapacitor electrode materials. ACS Appl. NANO Mater. 7 (22), 25628–25636.
Liu, M., Farhadi, B., Li, W., An, L., Li, Y., Zou, Z., Cong, Z., Zhai, S., An, Q., Wang, K., Tong, Y., 2024b. Nickel-cobalt layer double hydroxide @ lignin-based hollow carbon quasi core-shell structure for high-performance supercapacitors. Electrochim. Acta 478, 143836.
Liu, B.-L., Ma, Y.-X., Wang, J.-W., Kang, X.-Y., He, L.-J., Lei, L., Ran, F., 2022. Fabrication of nickel cobalt bimetallic sulfide doped graphite carbon nanohybrids as electrode materials for supercapacitors. Diam. Relat. Mater. 124, 108955.
Luo, L., Luo, L., Deng, J., Chen, T., Du, G., Fan, M., Zhao, W., 2021a. High performance supercapacitor electrodes based on B/N Co-doped biomass porous carbon materials by KOH activation and hydrothermal treatment. Int. J. Hydrog. Energy 46 (63), 31927–31937.
Luo, L., Wang, S., Zhou, Y., Yan, W., Gao, H., Luo, L., Deng, J., Du, G., Fan, M., Zhao, W., 2022. Microwave-assisted synthesis of hybrid supercapacitors consisting of Ni, Co-layered double hydroxide shell assembled around wood-derived activated carbon fiber core. Electrochim. Acta 412, 140148.
Luo, L., Zhou, Y., Yan, W., Luo, L., Deng, J., Du, G., Fan, M., Zhao, W., 2021b. Design and construction of hierarchical sea urchin-like NiCo-LDH@ACF composites for high-performance supercapacitors. Ind. Crops Prod. 171, 113900.
Maity, C.K., Sahoo, S., Verma, K., Behera, A.K., Nayak, G.C., 2020. Facile functionalization of boron nitride (BN) for the development of high-performance asymmetric supercapacitors. N. J. Chem. 44 (19), 8106–8119.
Nithya, V.D., 2021. A review on holey graphene electrode for supercapacitor. J. Energy Storage 44, 103380.
Perez-Gonzalez, R., Peng, Z., Camacho, D., Oliva, A.I., Oliva, J., 2020. All solid state stretchable carbon nanotube based supercapacitors with controllable output voltage. J. Energy Storage 32, 101844.
Seenivasan, S., Adhikari, S., Sivagurunathan, A.T., Kim, D.H., 2025. Supercapatteries: unlocking the potential of battery-supercapacitor fusion. Energy &amp Environ. Sci. 18 (3), 1054–1095.
Tang, Y., Guo, W., Zou, R., 2022. Nickel-based bimetallic battery-type materials for asymmetric supercapacitors. Coord. Chem. Rev. 451, 214242.
Tang, P., Jing, P., Tan, W., Dou, Q., Yan, X., 2024. Ion-confined transport supercapacitors: the encounter with energy electronics. Mater. Today 74, 187–202.
Tavakoli, N., Pourfayaz, F., Mehrpooya, M., 2025. Tri-optimization of cost, power and efficiency of a waste biomass gasification integrated with a molten carbonate fuel cell by a combined approach. Energy 314, 134319.
Wan, H., Liu, J., Ruan, Y., Lv, L., Peng, L., Ji, X., Miao, L., Jiang, J., 2015. Hierarchical configuration of NiCo2S4 Nanotube@Ni–Mn layered double hydroxide arrays/three-dimensional graphene sponge as electrode materials for high-capacitance supercapacitors. ACS Appl. Mater. & Interfaces 7 (29), 15840–15847.
Wang, S., Deng, J., Li, M., Lin, J., Luo, L., Yuan, Z., Zhang, W., He, C., Du, G., Zhao, W., 2025b. Nitrogen-Doped tannin carbon dots anchored NiCo-LDH composites for high-performance asymmetric supercapacitors. Chem. Eng. J. 511, 162275.
Wang, X., Ding, H., Luo, W., Yu, Y., Chen, Q., Luo, B., Xie, M., Guo, X., 2023b. Morphology evolution of CoNi-LDHs synergistically engineered by precipitant and variable cobalt for asymmetric supercapacitor with superior cycling stability. EcoEnergy 1 (2), 448–459.
Wang, S., Lin, J., Yuan, Z., Luo, L., Zhang, W., He, C., Zhao, W., 2025a. Tunable architecture of cobalt-nickel metal-organic framework/activated carbon composites for superior electrochemical performance in asymmetric supercapacitors. J. Colloid Interface Sci. 684, 647–657.
Wang, Y., Tang, H., Feng, H., Chai, D.-F., Zhang, W., Han, X., Li, Y., Dong, G., Guo, D., 2025a. d-d orbital interactions and spin-state modulation drive extensive surface reconstruction in chromium-incorporated layered double hydroxides for enhanced electrocatalytic oxygen evolution. Appl. Catal. B Environ. Energy 379, 125681.
Wang, B., Wang, C., Wang, Z., Ni, S., Yang, Y., Tian, P., 2023a. Adaptive state of energy evaluation for supercapacitor in emergency power system of more-electric aircraft. Energy 263, 125632.
Wang, C., Zhang, W., Qiu, X., Xu, C., 2024. Hydrothermal treatment of lignocellulosic biomass towards low-carbon development: Production of high-value-added bioproducts. EnergyChem 6 (6), 100133.
Xia, C., Jiang, Q., Zhao, C., Beaujuge, P.M., Alshareef, H.N., 2016. Asymmetric supercapacitors with metal-like ternary selenides and porous graphene electrodes. Nano Energy 24, 78–86.
Xie, M., Xu, Z., Duan, S., Tian, Z., Zhang, Y., Xiang, K., Lin, M., Guo, X., Ding, W., 2018. Facile growth of homogeneous Ni(OH)2 coating on carbon nanosheets for high-performance asymmetric supercapacitor applications. Nano Res. 11 (1), 216–224.
Yang, Y.J., Li, W., 2023. One step synthesis of NiCo-LDH/CoNi2S4/rGO composite on Ni foam for asymmetric supercapacitor. Fuller. Nanotub. Carbon Nanostruct. 31 (4), 327–335.
Yao, Y., Li, H., Yu, Y., Du, C., Wan, L., Ye, H., Chen, J., Zhang, Y., Xie, M., 2023b. Stabilizing microstructure of Co-Ni layered double hydroxides by magnesium doping and confinement in carbonaceous mesopores for ultrahighly-stable asymmetric supercapacitor. J. Energy Storage 59, 106422.
Yao, Y., Yu, Y., Wan, L., Du, C., Zhang, Y., Chen, J., Xie, M., 2023a. Structurally-stable Mg-Co-Ni LDH grown on reduced graphene by ball-milling and ion-exchange for highly-stable asymmetric supercapacitor. J. Colloid Interface Sci. 649, 519–527.
Yin, J., Zhou, G., Gao, X., Chen, J., Zhang, L., Xu, J., Zhao, P., Gao, F., 2019. α- and β-Phase Ni-Mg Hydroxide for High Performance Hybrid Supercapacitors. Nanomaterials 9 (12), 1686.
Zhang, P., Chen, Y., Song, X., Zhang, H., Cui, J., Wang, B., 2025a. Preparation of hierarchical porous carbon from corncob hydrochar by KCl enhancing K2CO3 activation for electrode material of supercapacitor. Chem. Eng. J. 503, 157703.
Zhang, Q., Wang, S., Lan, Y., Deng, J., Fan, M., Du, G., Zhao, W., 2024. Enhancing supercapacitor electrochemical performance through acetate-ion intercalation in layered nickel–cobalt double hydroxides. J. Colloid Interface Sci. 660, 597–607.
Zhang, Z., Zhao, Y., Yin, J., Li, H., 2025b. Construction of CoWO4/CoNiFe-LDH heterostructure for enhanced capacitive performance of asymmetric supercapacitors. J. Alloy. Compd. 1045, 184795.
Zhao, W., Deng, J., Li, M., Du, G., Fan, M., Gao, H., Yuan, Z., 2025. Rational synthesis of sea urchin-like NiCo-LDH/tannin carbon microsphere composites using microwave hydrothermal technique for high-performance asymmetric supercapacitor. Adv. Compos. Hybrid. Mater. 8 (2), 215.
Zhao, W., Deng, J., Zhang, Q., Luo, L., Luo, L., Wang, H., Lin, J., Gao, H., 2026. Sustainable balsa-derived polyaniline/activated carbon composites for high-performance asymmetric supercapacitors. J. Energy Storage 146, 120072.
Zhou, Y., Yan, W., Yu, X., Chen, T., Wang, S., Zhao, W., 2020. Boron and nitrogen co-doped porous carbon for supercapacitors: A comparison between a microwave-assisted and a conventional hydrothermal process. J. Energy Storage 32, 101706.